Quantum-accurate spectral neighbor analysis potential models for Ni-Mo binary alloys and fcc metals

Xiang-Guo Li, Chongze Hu, Chi Chen, Zhi Deng, Jian Luo, and Shyue Ping Ong*
Department of NanoEngineering, University of California San Diego, 9500 Gilman Drive, Mail Code 0448, La Jolla, California 92093-0448, USA

(Received 12 June 2018; revised manuscript received 8 August 2018; published 11 September 2018)

In recent years, efficient interatomic potentials approaching the accuracy of density functional theory (DFT) calculations have been developed using rigorous atomic descriptors satisfying strict invariances, for example, for translation, rotation, permutation of homonuclear atoms, among others. In this paper, we generalize the spectral neighbor analysis potential (SNAP) model to bcc-fcc binary alloy systems. We demonstrate that machine-learned SNAP models can yield significant improvements even over the well-established high-performing embedded atom method (EAM) and modified EAM potentials for fcc Cu and Ni. We also report on the development of a SNAP model for the fcc Ni-bcc Mo binary system by machine learning a carefully constructed large computed data set of elemental and intermetallic compounds. We demonstrate that this binary Ni-Mo SNAP model can achieve excellent agreement with experiments in the prediction of a Ni-Mo phase diagram as well as near-DFT accuracy in the prediction of many key properties, such as elastic constants, formation energies, melting points, etc., across the entire binary composition range. In contrast, the existing Ni-Mo EAM has significant errors in the prediction of the phase diagram and completely fails in binary compounds. This paper provides a systematic model development process for multicomponent alloy systems, including an efficient procedure to optimize the hyperparameters in the model fitting, and paves the way for long-time large-scale simulations of such systems.

DOI: 10.1103/PhysRevB.98.094104

I. INTRODUCTION

Machine learning (ML) models based on robust local environment descriptors have recently emerged as an approach to describe the potential-energy surface (PES) of systems of atoms with near-quantum accuracy at several of orders magnitude lower cost than *ab initio* methods [1–6]. Effective local environment descriptors must be invariant under translation, rotation, and permutation of homonuclear atoms and have the properties of uniqueness and differentiability [7]. Examples of such descriptors include symmetry functions [1,8], smooth overlap of atomic positions (SOAPs) [4,9], the bispectrum [2,5], the Coulomb matrix [3,10,11], among others. A typical approach is to fit the PES as a function of these descriptors by machine learning on *ab initio* data sets, using techniques ranging from simple linear regression [5,12] to kernel ridge regression [6,7] to neural networks [13–16].

Thus far, the development of ML potentials based on local environment descriptors has largely been limited to elements and oxides. The Gaussian approximation potential using the SOAP descriptor has been applied on Si [4], C [17,18], W [9], P [19], and Fe [20], and neural network models based on symmetry functions have been fitted for Si [21], C [22], Na [23], ZnO [24], TiO_2 [25], GeTe [26], and Li_3PO_4 [27]. Thompson *et al.* [5] and Wood and Thompson [28] have developed linear and quadratic models based on the SO(4) bispectrum—the spectral analysis neighbor potential (SNAP)—for bcc Ta and W. Chen *et al.* [12] later showed that a linear SNAP model can achieve near- density functional theory (DFT) accuracy across a wide range of properties and outperforms the embedded atom method (EAM) and modified EAM (MEAM) in the bcc Mo system. Only recently, neural network models utilizing the symmetry function descriptors have been extended to Al-Mg-Si [29] and Li_xSi [30] alloy systems. The extension of ML models to multicomponent oxides and alloys generally leads to a large expansion in the size of the descriptor feature vector and, correspondingly, an explosion in the quantity of data (and hence computational cost) necessary for model fitting.

In this paper, we will apply the linear SNAP approach to the bcc Mo-fcc Ni binary alloy system as well as present an investigation of its performance on fcc metals (Cu and Ni). Our choice of model is motivated by the relatively simple functional form of the linear SNAP approach, which reduces the computational effort for model training and minimizes the risk of overfitting. Although Wood and Thompson [28] have recently shown a quadratic SNAP model can achieve higher accuracies, this improvement comes at a large increase in the number of fitted coefficients (e.g., 481 for quadratic SNAP vs 31 for linear SNAP in Ta) and, consequently, a large increase in the training data set required, an issue which is severely exacerbated in multicomponent systems. On the other hand, the efficiency of the Gaussian approximation potential based on the SOAP descriptor [9] depends on the size of the underlying reference set, which would again be greatly compounded in a multicomponent system. Ni-Mo alloys are

*ongsp@eng.ucsd.edu

of immense technological interest due to their high corrosion resistance, low thermal-expansion coefficients, and hardness and catalytic properties [31–34]. The currently available Ni-Mo EAM force field cannot provide satisfactory accuracy on many properties and even fails in binary compounds. We demonstrate that the ML SNAP models for both fcc and fcc-bcc mixed binary systems can achieve near-quantum accuracy across a wide range of properties, including energies, forces, elastic properties, melting points, surface energy, etc., consistently outperforming the EAM models especially in the binary systems.

II. METHODS

A. Bispectrum and SNAP formalism

The bispectrum and SNAP formalism have been extensively covered in previous works [2,5]. We will only briefly describe the key concepts here for completeness.

The atomic environment is described by the neighbor density $\rho_i(\mathbf{r})$ for each atom i at coordinates $\mathbf{r}$, defined as follows:

$$\rho_i(\mathbf{r}) = \delta(\mathbf{r}) + \sum_{r_{ij}<R_c} f_c(r_{ij}) w^j_{\text{atom}} \delta(\mathbf{r} - \mathbf{r}_{ij}), \tag{1}$$

where $\delta(\mathbf{r} - \mathbf{r}_{ij})$ is the Dirac δ function centered at each neighboring site, the cutoff function f_c ensures a smooth decay for the neighbor atomic density to zero at the cutoff radius R_c, and the dimensionless atomic weights w^j_{atom} distinguish different atom types. This density function can then be expanded in four-dimensional hyperspherical harmonics $U^j_{m,m'}(\theta, \phi, \theta_0)$ as

$$\rho_i(\mathbf{r}) = \sum_{j=0}^{\infty} \sum_{m,m'=-j}^{j} u^j_{m,m'} U^j_{m,m'}(\theta, \phi, \theta_0). \tag{2}$$

where the radial component is converted into a third polar angle defined by $\theta_0 = \theta_0^{\max} \frac{r}{R_c}$, $\theta_0^{\max}$ is the angle conversion function, which was kept at the default value of $0.993\,63\pi$ in this paper, and the coefficients $u^j_{m,m'}$ are given by the inner product $\langle U^j_{m,m'} | \rho \rangle$. The bispectrum coefficients are then given by

$$\boldsymbol{B}_{j_1,j_2,j} = \sum_{m_1,m_1'=-j_1}^{j_1} \sum_{m_2,m_2'=-j_2}^{j_2} \sum_{m,m'=-j}^{j} \times \left(u^j_{m,m'}\right)^* C^{jm}_{j_1 m_1 j_2 m_2} C^{jm'}_{j_1 m_1' j_2 m_2'} u^{j_1}_{m_1',m_1} u^{j_2}_{m_2',m_2}, \tag{3}$$

where $C^{jm}_{j_1 m_1 j_2 m_2}$'s are Clebsch-Gordon coefficients. In practice, j, j_1, and j_2 need to be truncated with $j, j_1, j_2 \leqslant j_{\max}$. We found that an order of three for the bispectrum coefficients ($j_{\max} = 3$) is sufficient based on our tests, consistent with previous works [2,5,12], which gives a total of 31 projected bispectrum components.

In the SNAP formalism, the total energy E_{SNAP} and forces F_{SNAP} are expressed as a linear function of the 31 projected bispectrum components B_k ($k = \{j, j_1, j_2\}$) and their derivatives as follows:

$$E_{\text{SNAP}} = \sum_{i=1}^{N} \beta_0^{\alpha_i} + \sum_{i=1}^{N} \sum_{k=\{j,j_1,j_2\}} \beta_k^{\alpha_i} B_k^i, \tag{4}$$

$$\boldsymbol{F}^j_{\text{SNAP}} = -\sum_{i=1}^{N} \boldsymbol{\beta}^{\alpha_i} \cdot \frac{\partial \boldsymbol{B}^i}{\partial \mathbf{r}_j}, \tag{5}$$

where $\beta_k^{\alpha_i}$'s are the fitting parameters in the linear model and α_i specifies the atom type of atom i.

The calculations of bispectrum coefficients (the features) for all the training structures were performed using the implementation in the LAMMPS software [35]. The cutoff radius R_c and atomic weight w_{atom} were treated as hyperparameters fitted during the training of the model as outlined in subsequent sections.

B. SNAP model fitting

For elemental fcc systems, we adopted the potential fitting work flow developed in Ref. [12] as shown in the left panel of Fig. 1. We denote this whole optimization process as one optimization unit, which consists of two optimization loops. The inner loop optimizes the ML model parameters by mapping the descriptors (bispectrum coefficients) to DFT energies and forces. The outer loop optimizes the hyperparameters by minimizing the difference between the model predicted material properties, i.e., elastic tensors, and the DFT computed values. As introduced in Ref. [12], the hyperparameters are the data weights (ω) from different data groups, and the parameters (α) used in bispectrum calculations, i.e., the radius cutoff R_c and atomic weight w_{atom}. In the elemental system, the atomic weight can be set as unity. The inner loop fitting of the model coefficients was performed with the least-squares algorithm implemented in the SCIKIT-LEARN package [36]. The outer loop optimization was performed using the differential evolution algorithm [37] from the SCIPY package [38].

For the binary Ni-Mo alloy system, there are four parameters (R_c^{Ni}, R_c^{Mo}, $w^{i,\text{Ni}}_{\text{atom}}$, $w^{j,\text{Mo}}_{\text{atom}}$) in the bispectrum calculations, two for each element. As it would be far too time consuming to optimize all parameters simultaneously, we propose instead a two-step model fitting work flow as shown in the right panel of Fig. 1. The first step involves the independent optimization of the radius cutoff R_c for each elemental system, i.e., Ni and Mo. The maximum of the two optimized radius cutoffs $\max(R_c^{\text{Ni}}, R_c^{\text{Mo}})$ is then used as a common radius cutoff for the binary Ni-Mo system. The use of a common radius cutoff is to maintain symmetric interactions between neighboring atoms of different types, i.e., the interaction between a Mo and a neighboring Ni should be the same as that between a Ni and a neighboring Mo for the same distance. The atomic weight for the element with the larger radius cutoff (Mo in this case) is then set at unity. Therefore, only one parameter, the atomic weight for the other element, needs to be optimized in the second optimization step as shown in the right panel of Fig. 1.

C. Training data generation

A diverse set of the training data encompassing a good range of atomic local environments is critical to developing an

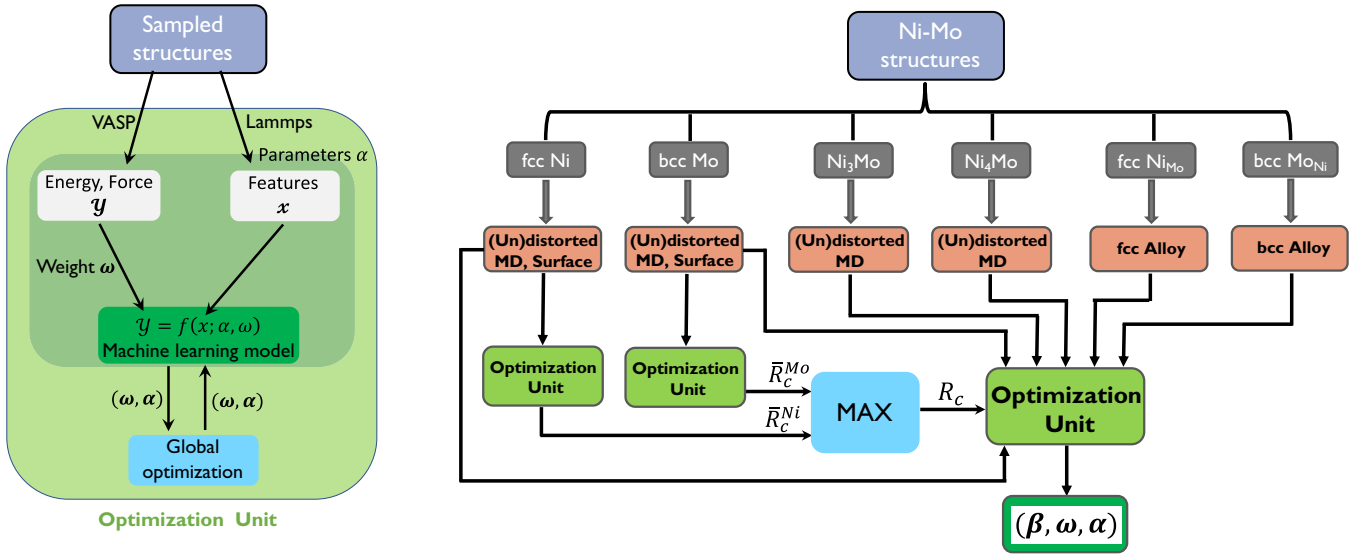

FIG. 1. Fitting work flow for the binary alloy SNAP model. The left panel shows one optimization unit developed by Chen *et al.* [12], which optimizes both the model parameters and the hyperparameters with respect to DFT calculated energies, forces, and elastic constants. The right panel shows the work flow for the binary alloy system. α denotes the parameters (hyperparameters) for the bispectrum calculations, whereas β denotes the model parameters.

effective and robust potential. Our training data can be divided into five categories:

(1) Undistorted ground-state structures for Ni, Mo, and the two binary intermetallics Ni_3Mo and Ni_4Mo.

(2) Distorted structures constructed by applying strains of -10% to 10% at 1% intervals to a bulk supercell in six different modes as described in Ref. [39].

(3) Surface structures of elemental structures obtained from the Crystalium database [40], which include the surface structures with Miller indices up to three.

(4) Snapshots from NVT *ab initio* molecular dynamics (AIMD) simulations of the bulk supercell at 300, 1000, and 3000 K at the equilibrium 0-K volume. In addition, snapshots were also obtained from NVT AIMD simulations at 300 K at 90% and 110% of the equilibrium 0-K volume. Forty snapshots were extracted from each AIMD simulation at intervals of 0.1 ps.

(5) Alloy structures constructed by partial substitution of supercells of the bulk fcc Ni with Mo and the bulk bcc Mo with Ni. Compositions of the form Ni_xMo_{1-x} were generated with x ranging from 0 to 100 at. % at intervals of 12.5 at. %.

The supercells used for the distorted structures and AIMD simulations are $3 \times 3 \times 3$ conventional cells for all elemental systems, $3 \times 3 \times 2$ for Ni_3Mo, and $2 \times 2 \times 3$ for Ni_4Mo. The Mo-substituted Ni fcc alloy (Ni_{Mo}) structures were generated in three steps. First, a $2 \times 2 \times 2$ supercell of Ni was doped with 1–5, 9, 13, 17, 21, 25, 29, 30–32 Mo atoms, respectively. Second, for each doped structure, we performed a structure enumeration [41] to generate all symmetrically distinct structures from which up to 100 random structures are selected. Third, we performed a structure relaxation for each selected structure. Both the unrelaxed and the relaxed structures were included in our data set. The Ni-substituted Mo bcc alloy (Mo_{Ni}) structures were constructed using the same procedure with a $2 \times 2 \times 2$ supercell. In addition, since the bcc conventional cell contains half the number of atoms of the fcc conventional cell, we also generated low-concentration Ni-substituted Mo by doping a $3 \times 3 \times 3$ Mo supercell with one to four Ni atoms.

D. DFT calculations

All DFT calculations were performed using the Perdew-Burke-Ernzerhof [42] exchange-correlation functional as implemented in the Vienna *ab initio* simulation package (VASP) [43] within the projector augmented-wave approach [44]. The kinetic-energy cutoff was set to 520 eV, and the k-point density was at least 3000 per reciprocal atom. Energies and forces were converged to within 10^{-5} eV and 0.02 eV/Å, respectively. The AIMD simulations were performed with a single Γ k point and were nonspin polarized. However, the energy and force calculations on the snapshots were performed using the same parameters as the rest of the data. All structure manipulations and analyses of DFT computations were carried out using the Python Materials Genomics [45] library, and the automation of the calculations was carried out using the FIREWORKS software [46].

E. Melting points and phase diagram

The melting temperatures T_m were calculated using the solid-liquid coexistence approach [47]. MD simulations were performed using the $30 \times 15 \times 15$ bcc (13 500 atoms) and $30 \times 10 \times 10$ (12 000 atoms) fcc supercells under zero pressure at different temperatures. The time step was set to 1 fs, and simulations were carried out for at least 100 ps. T_m was identified when the initial solid and liquid phases were at equilibrium (no interface motion).

With the fully equilibrated solid-liquid structures at the melting points, we conducted hybrid Monte Carlo (MC)/MD simulations to calculate the solidus and liquidus lines at different temperatures. At each temperature below T_m, the global

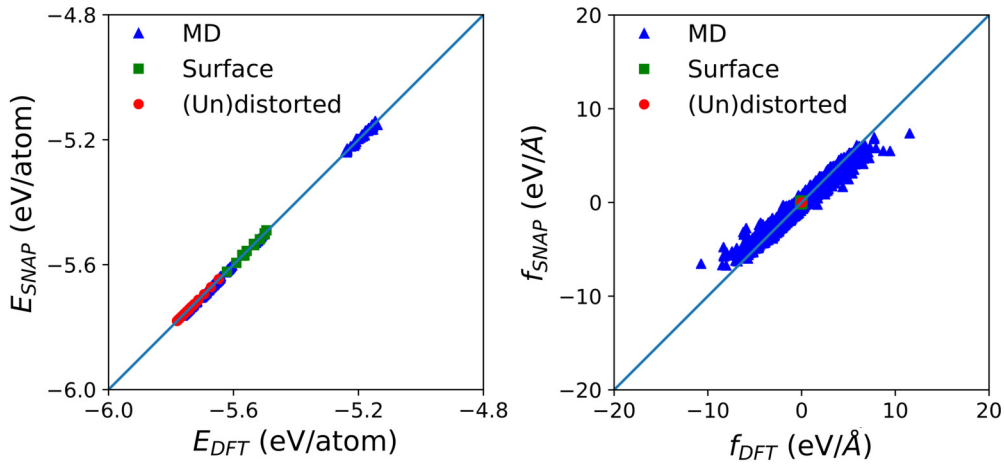

FIG. 2. Plot of SNAP predictions vs DFT for energies (left panel) and forces (right panel) in the elemental Ni system for different data groups. The mean absolute errors (MAEs) for energy and force are 1.2 meV/atom and 0.05 eV/Å, respectively.

composition of dopant atoms was adjusted to find solid-liquid equilibrium phases. The solidus and liquidus lines were then determined by calculating the composition of dopant atoms in the solid and liquid phases, respectively. To reduce statistical errors, all calculations were averaged based on five random structures in the last 10 ps.

The calculation of the phase diagrams (CALPHAD) Ni-Mo phase diagram [48] was constructed using the PANDAT software [49]. In the CALPHAD approach, the liquid phase and two solid terminal phases of the Ni-Mo alloy were treated using a subregular solution model [50], and the model parameters were fitted to experimental data on phase equilibria in the Mo-Ni system.

F. Data availability

To ensure the reproducibility and use of the models developed in this paper, all data (structures, energies, forces, etc.) used in model development as well as the final fitted model coefficients have been published in an open repository [51]. We will also work with the developers of LAMMPS to include the elemental and binary SNAP models in the LAMMPS software package.

III. RESULTS

A. Optimized SNAP model coefficients

The optimized SNAP model coefficients [β_k in Eq. (5)] for elemental fcc Ni, Cu, and mixed bcc Ni-fcc Mo systems are provided in the Supplemental Material [52]. The optimized elemental cutoff radius R_c^{Ni} and R_c^{Cu} are 3.9 and 3.7 Å, respectively, slightly larger than the second-nearest-neighbor distance in the respective fcc crystals. For bcc Mo, the optimized R_c^{Mo} is 4.6 Å [12]. For the mixed bcc Ni-fcc Mo model, the overall cutoff radius R_c is set as $\max(R_c^{\mathrm{Ni}}, R_c^{\mathrm{Mo}}) = 4.6$ Å, $w_{\mathrm{atom}}^{\mathrm{Mo}} = 1.0$, and the optimized value for $w_{\mathrm{atom}}^{\mathrm{Ni}}$ is 0.5.

B. Performance of the fcc Ni SNAP model

We will first discuss the performance of the SNAP model for fcc metals, given that the SNAP approach has hitherto been applied to only bcc metals, such as W, Ta, and Mo. Here, we will focus our discussion on the elemental fcc Ni SNAP model and compare its performance to that for the binary fcc Ni-bcc Mo model. We have constructed a SNAP model for Cu as well using a similar approach and compared its elastic properties with experiment [53]. The qualitative results are similar with Ni and reported in the Supplemental Material [52].

1. Energies and forces

A comparison of the DFT and SNAP predicted energies and forces for elemental Ni is shown in Fig. 2. For both energies and forces, SNAP model predictions are in line with the DFT results with a unity slope. EAM potentials are well known to have a good performance in fcc metals [54]. The MAE in the energies and forces (relative to DFT) for the EAM potential [55] are 10.6 meV/atom and 0.06 eV/Å, respectively, whereas that for the MEAM potential [56] are 17.8 meV/atom and 0.08 eV/Å, respectively. The Ni SNAP model can achieve a much lower MAE in energy of 1.2 meV/atom and slightly improved MAE in the force of 0.05 eV/Å.

To further validate our model, we generated test structures by performing additional Ni surface calculations with Miller indices up to four and extracting 40 snapshots from AIMD simulations on the vacancy-containing supercell of Ni at 1000 K. The predicted MAEs for the energies and forces are 2.3 meV/atom and 0.08 eV/Å, respectively, comparable to the model performance on the training data sets. This validation of the model on previous unseen data indicates that the model can be generalized.

2. Materials properties

Table I provides a comparison of the Ni SNAP model predictions of the melting points and elastic properties with DFT, EAM/MEAM potentials, and experiments [58]. We find that both the SNAP and the MEAM models predict melting points that are in excellent agreement (within 2% to 3%) with the experimental value, but the EAM model greatly underestimates the melting point by ∼12%. The Ni elastic moduli predicted by the SNAP model are in extremely good agreement with the DFT, but those predicted by the MEAM model are much

TABLE I. Comparison of the calculated and experimental melting points (T_m), elastic constants (c_{ij}), Voigt-Reuss-Hill [57] bulk modulus (B_{VRH}), shear modulus (G_{VRH}), Poisson's ratio (μ), vacancy formation energy (E_v), and migration energy (E_m) of fcc Ni. Error percentages of the SNAP, EAM, and MEAM predictions with respect to DFT values are shown in parentheses. The values of B_{VRH}, G_{VRH}, and μ in the Expt. column are derived from the experimental elastic constants.

	DFT	SNAP	EAM [55]	MEAM [56]	Expt.
T_m (K)		1785	1520	1765	1728
c_{11} (GPa)	276	276 (0.0%)	248 (−10.1%)	260 (−5.8%)	261 [58]
c_{12} (GPa)	159	159 (0.0%)	147 (−7.5%)	151 (−7.5%)	151 [58]
c_{44} (GPa)	132	132 (0.0%)	125 (−5.3%)	131 (−0.8%)	132 [58]
B_{VRH} (GPa)	198	198 (0.0%)	181 (−8.6%)	187 (−5.6%)	188
G_{VRH} (GPa)	95	95 (0.0%)	87 (−8.4%)	92 (−3.2%)	93
μ	0.29	0.29 (0.0%)	0.29 (0.0%)	0.29 (0.0%)	0.29
E_v (eV)	1.46	1.68 (15.1%)	1.68 (15.1%)	1.16 (−20.5%)	1.54–1.80 [59]
E_m (eV)	1.12	1.07 (−4.5%)	0.90 (−19.6%)	1.46 (30.4%)	1.01–1.48 [59]
$E_a = E_v + E_m$ (eV)	2.58	2.75 (6.6%)	2.58 (0%)	2.62 (1.6%)	2.77–2.95 [59]

closer to the experimental values. These differences are the result of the data used for model fitting—the SNAP model was fitted using DFT-calculated data, whereas the MEAM model [56] was fitted using the experimental elastic moduli. The EAM-predicted elastic moduli deviate significantly from both the DFT and the experimental values. The SNAP model also predicts vacancy formation and migration energies [60] that are much closer to the DFT values. The EAM model greatly underestimates E_m by ∼20%, whereas MEAM significantly overestimates E_m by more than 30%.

Figure 3 shows the equation of state curves constructed using the DFT, SNAP, EAM, and MEAM models. We observe that the SNAP curve overlaps with DFT for the whole covered region with volume changes in the range of −17% to 21% from the equilibrium volume. The EAM potential deviates significantly from the DFT curve at both tensile and compressive strains, and the MEAM potential slightly underestimates the energy at large compressive strains. By fitting the Murnaghan equation of state, the estimated bulk moduli from Fig. 3 are 188, 190, 160, and 177 GPa for DFT, SNAP, EAM, and MEAM, respectively. All three models (SNAP, EAM, and MEAM) lead to very similar phonon dispersion curves that are slightly underestimated relative to the DFT curves (see Fig. S3 in the Supplemental Material [52]).

Figure 4 compares the performance of the Ni SNAP model with DFT [40] and the EAM/MEAM models in the prediction of Ni surface energies up to a maximum Miller index of four. The surface energies computed by the SNAP model are in excellent agreement with the DFT calculations, whereas both the EAM and the MEAM models significantly underestimate surface energies. It should be noted that the surfaces with Miller indices beyond three, e.g., (411), (421), etc., are not part of the training data set and constitute test data that further validate the applicability of the SNAP model beyond already-seen data.

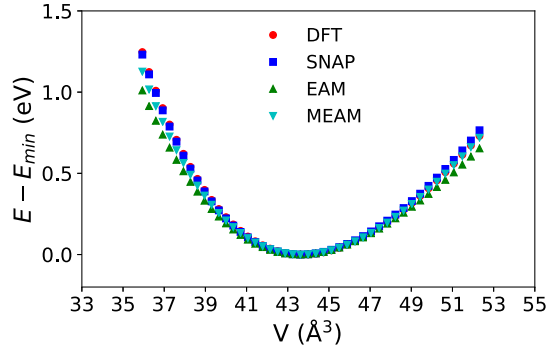

FIG. 3. Energy vs volume curves of a conventional fcc Ni cell for the DFT, SNAP, EAM, and MEAM models. The energy at the equilibrium volume has been set as the zero reference.

C. Performance of the binary Ni-Mo SNAP model

In this section, we will discuss the performance of the optimized binary Ni-Mo SNAP model. We will not only compare the performance of the binary SNAP model to DFT and EAM, but also compare the performance of the binary SNAP model relative to the optimized elemental Ni and Mo SNAP models and discuss any compromises in the performance on the elemental end members in going from a single component to a binary model.

1. Energies and forces

Table II compares the MAEs in predicted energies and forces relative to DFT for the elemental and binary Ni-Mo

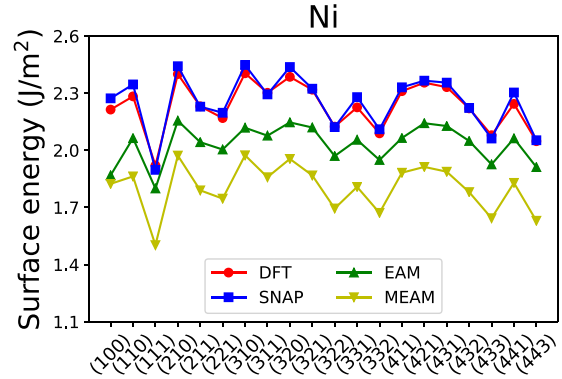

FIG. 4. Comparison of calculated surface energies for Ni surfaces with Miller indices up to a maximum of four using DFT, SNAP, EAM, and MEAM.

TABLE II. Comparison of the MAEs in predicted energies and forces relative to DFT for the three SNAP models (elemental Ni, elemental Mo [12], and binary Ni-Mo) and the binary Ni-Mo EAM model [55]. The "Overall" column refers to the MAE across the entire training data set.

	Model	Mo	Ni_4Mo	Ni_3Mo	Mo_{Ni}	Ni_{Mo}	Ni	Overall
Energy (meV/atom)	Ni SNAP						1.2	
	Mo SNAP	13.2						
	Ni-Mo SNAP	16.2	4.0	5.2	22.7	33.9	7.9	22.5
	EAM	58.9	211.2	255.6	46.5	147.6	10.6	117.2
Force (eV/Å)	Ni SNAP						0.05	
	Mo SNAP	0.25						
	Ni-Mo SNAP	0.29	0.14	0.16	0.13	0.55	0.11	0.23
	EAM	0.31	0.20	0.19	0.21	0.57	0.06	0.26

SNAP models and the binary Ni-Mo EAM model [55]. It should be noted that the binary EAM model was constructed from normalized elemental EAM potentials with a relative scaling factor between elements. The relative scaling factor along with the EAM parameters are fitted to the experimentally measured properties, such as lattice constants, elastic constants, vacancy formation energies, heats of solution, etc. As such, our discussion of the relative performance of the

TABLE III. Comparison of elastic constants (c_{ij}), Voigt-Reuss-Hill [57] bulk modulus (B_{VRH}), shear modulus (G_{VRH}), and Poisson's ratio (μ) for fcc Ni, bcc Mo, and binary compounds Ni_4Mo and Ni_3Mo. Error percentages of the SNAP (elemental Ni SNAP, Mo SNAP, and binary Ni-Mo SNAP) and EAM predictions relative to DFT values are shown in parentheses. The values of B_{VRH}, G_{VRH}, and μ in the Expt. column are derived from the experimental elastic constants.

	DFT	Mo SNAP [12]	Ni SNAP	Ni-Mo SNAP	EAM	Expt.
Mo						
c_{11} (GPa)	472	473 (0.2%)		475 (0.6%)	457 (−3.2%)	479 [61]
c_{12} (GPa)	158	152 (−3.8%)		163 (3.2%)	168 (6.3%)	165 [61]
c_{44} (GPa)	106	107 (0.9%)		111 (4.7%)	116 (9.4%)	108 [61]
B_{VRH} (GPa)	263	259 (−1.5%)		267 (1.5%)	264 (0.4%)	270
G_{VRH} (GPa)	124	126 (−1.6%)		127 (2.4%)	127 (2.4%)	125
μ	0.30	0.29 (−3.3%)		0.29 (−3.3%)	0.29 (−3.3%)	0.30
Ni						
c_{11} (GPa)	276		276 (0.0%)	269 (−2.5%)	248 (−10.1%)	261 [58]
c_{12} (GPa)	159		159 (0.0%)	150 (−5.7%)	147 (−7.5%)	151 [58]
c_{44} (GPa)	132		132 (0.0%)	135 (2.3%)	125 (−5.3%)	132 [58]
B_{VRH} (GPa)	198		198 (0.0%)	190 (−4.0%)	181 (−8.6%)	188
G_{VRH} (GPa)	95		95 (0.0%)	97 (2.1%)	87 (−8.4%)	93
μ	0.29		0.29 (0.0%)	0.28 (−3.4%)	0.29 (0.0%)	0.29
Ni_3Mo						
c_{11} (GPa)	385			420 (9.1%)	195 (−49.4%)	
c_{12} (GPa)	166			197 (18.7%)	98 (−41.0%)	
c_{13} (GPa)	145			162 (11.7%)	98 (−32.4%)	
c_{23} (GPa)	131			145 (10.7%)	107 (−18.3%)	
c_{22} (GPa)	402			360 (−10.4%)	98 (−12.7%)	
c_{33} (GPa)	402			408 (1.5%)	295 (−26.6%)	
c_{44} (GPa)	94			84 (−10.6%)	36 (−61.7%)	
B_{VRH} (GPa)	230			243 (5.7%)	156 (−32.2%)	
G_{VRH} (GPa)	89			100 (12.4%)	61 (−31.5%)	
μ	0.33			0.32 (−3.0%)	0.33 (0.0%)	
Ni_4Mo						
c_{11} (GPa)	300			283 (−5.7%)	172 (−42.7%)	
c_{12} (GPa)	186			179 (−3.8%)	158 (−15.1%)	
c_{23} (GPa)	166			164 (−1.2%)	80 (−51.8%)	
c_{22} (GPa)	313			326 (4.2%)	158 (−49.5%)	
c_{44} (GPa)	130			126 (−3.1%)	125 (−3.8%)	
B_{VRH} (GPa)	223			220 (−1.3%)	161 (−27.8%)	
G_{VRH} (GPa)	91			95 (4.4%)	−156 (−162%)	
μ	0.33			0.31 (−6.1%)	0.70 (112%)	

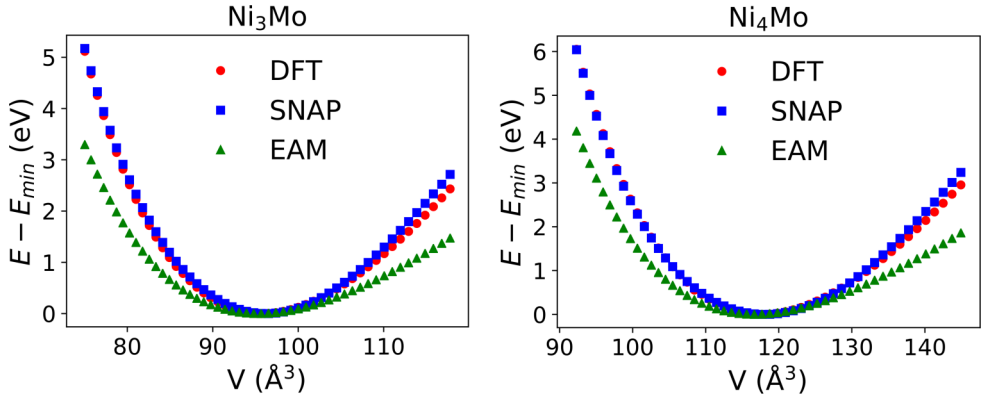

FIG. 5. Energy vs volume curves of a conventional Ni_3Mo (left panel) and Ni_4Mo (right panel) cell for the DFT, SNAP, and EAM models. The energy at the equilibrium volume has been set as the zero reference.

Ni-Mo SNAP and EAM models will focus on qualitative trends (especially in the binary alloys and intermetallics) rather than quantitative comparisons.

We may observe that the binary Ni-Mo SNAP model significantly outperforms the binary Ni-Mo EAM model across almost all data sets with the exception of a larger MAE in predicted forces for pure Ni. In particular, the MAEs in the predicted energies for the binary phases (Ni_4Mo, Ni_3Mo, and the Mo-doped fcc Ni) are especially large for the EAM model relative to the end member elemental phases, whereas those for the binary Ni-Mo SNAP are much smaller and comparable for both binary as well as elemental phases. This indicates a clear bias for the elemental phases in the construction of the binary EAM potential. However, relative to the elemental Mo and Ni SNAP models, the binary Ni-Mo SNAP model clearly sacrifices accuracy on the end member elements with somewhat larger errors in predicted energies and forces for both bcc Mo and fcc Ni. We attribute this decrease in accuracy to the substantially more complex and diverse training structures when fitting the binary potential compared with the elemental potential.

2. Materials properties

Table III compares the elastic properties computed by the elemental and binary SNAP models, the EAM model, DFT, and experiments [58,61]. Again, we observe that the binary Ni-Mo SNAP model generally outperforms the binary EAM model in the prediction of the elastic constants, bulk and shear moduli, and Poisson's ratio for the binary intermetallics Ni_3Mo and Ni_4Mo. The binary EAM model performs especially poorly in this regard with absolute percentage errors exceeding 100% in some instances (e.g., shear modulus and Poisson's ratio for Ni_4Mo). Compared to the elemental SNAP models, the binary Ni-Mo SNAP model does suffer a slight decrease in prediction accuracy but still manages to retain better agreement with DFT compared with EAM.

Figure 5 displays the equation of state curves constructed using the DFT, SNAP, and EAM models for the binary compounds Ni_3Mo and Ni_4Mo. We observe that for both Ni_3Mo and Ni_4Mo, the SNAP curve overlaps with DFT for volume changes in the range of -21% to 10% from the equilibrium volume but begins to slightly overestimate the energies with volume expansions beyond 10%. The EAM potential completely fails in the equation of state prediction for binary compounds. It significantly underestimates the energies at both tensile and compressive strains. Similar conclusions can be made from the prediction of the phonon dispersion curves—the binary SNAP model produces phonon dispersion curves that are in excellent agreement with DFT for both Ni_3Mo and Ni_4Mo, whereas the EAM potential produces curves with imaginary frequencies, in contradiction to DFT (see Fig. S4 in the Supplemental Material [52]).

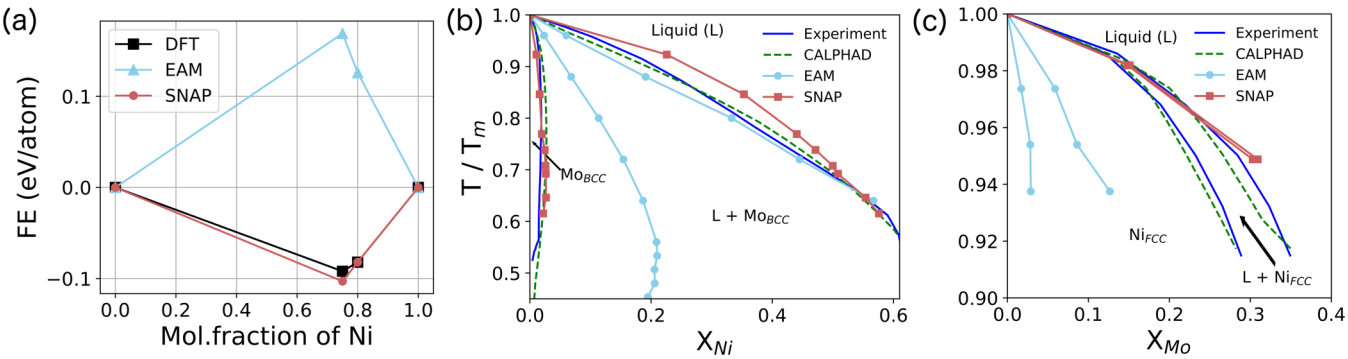

FIG. 6. Plots of the (a) 0-K Ni-Mo pseudobinary formation energy diagram calculated using DFT, SNAP, and EAM, and the high-temperature Ni-Mo phase diagram normalized by the melting temperature for (b) the Mo-rich domain and (c) the Ni-rich domain from experiments [62], CALPHAD, SNAP, and EAM models.

TABLE IV. Melting temperatures (in kelvins) for pure Mo and Ni with different methods. EAM and SNAP values are calculated using the binary force field.

	Experiment	CALPHAD	EAM	SNAP
Pure Mo	2898	2899	3750	3250
Pure Ni	1728	1728	1520	1810

Figure 6(a) compares the 0-K Ni-Mo pseudobinary formation energy diagram calculated using DFT and the binary SNAP and EAM models. The binary EAM model fails to reproduce even qualitatively the convex hull, predicting positive formation energies for Ni_3Mo and Ni_4Mo, whereas the binary SNAP model predictions are in good agreement with DFT. This is consistent with the large prediction error in the energies of the binary intermetallics for the EAM model discussed in the previous section.

Figures 6(b) and 6(c) compare the high-temperature (>1000-K) Ni-Mo phase diagram normalized by the melting temperature calculated from hybrid MC-MD simulations using the binary SNAP and EAM models with those from experiments and CALPHAD [62]. Again, we note that the EAM calculated phase diagram exhibits large errors, greatly overestimating the solubility of Ni in Mo by more than ten times and the melting point of Mo by about 29.4% (see Table IV). In contrast, the SNAP model predicts a maximum solubility of Ni in Mo of about 2.6% for SNAP, which is in excellent agreement with the experimental value of 1.9%, and the predicted melting points for Mo are also closer to the experimental values (12.2% higher, see Table IV). The liquidus line calculated by SNAP exhibits concavelike transitions with temperatures, consistent with the experimental phase diagram, but EAM gives a linear relationship. At the Ni-rich domain, the experimental and CALPHAD liquidus and solidus lines are almost overlapping with each other close to T_m of Ni, and this behavior is successfully reproduced by the SNAP model. EAM, on the other hand, shows a large segregation to liquid phases as the temperature decreases from T_m, contradictory to experiment. In addition, the solubility of Mo in Ni predicted by EAM is only about one-tenth of the experimental value. The main major discrepancy for the binary SNAP model is in the separation of the solidus and liquidus lines. The binary SNAP model predicts an extremely small separation between the solidus and the liquidus lines as the temperature is decreased from the Ni melting point, whereas experimentally, these lines are separated by ∼5% Ni.

IV. DISCUSSION AND CONCLUSION

To conclude, we have developed SNAP models for fcc Ni, Cu, as well as the binary Ni-Mo system.

For fcc metals, such as Ni and Cu, we find that the elemental SNAP models offer only a modest improvement over well-established EAM/MEAM potentials. This is unlike the case for bcc metals, such as Mo, Ta, and W for which EAM/MEAM potentials generally perform relatively poorly and SNAP models have been demonstrated to lead to significant reductions in prediction error in energies, forces, and various materials' properties [5,12,28].

Where the SNAP formalism truly shines is its extensibility to multicomponent systems, achieving consistently low and comparable MAEs in the energies and forces for the elemental end members as well as the binary intermetallics and solid solutions for the bcc Mo-fcc Ni binary alloy system. This performance is achieved using the same simple linear model with a doubling of the number of fitted coefficients and hyperparameters. We have proposed a two-step fitting approach to efficiently determine the hyperparameters. In contrast, the EAM model is significantly biased for better error performance in the elemental end members with extremely large errors and failing even on a qualitative level for the binary intermetallics and alloys. We have successfully applied this SNAP model to reproduce the high-temperature Ni-Mo phase diagram in excellent agreement with experiments. We believe SNAP models developed using the same principles and approach can enable high accuracy studies of microstructure and other phenomena requiring large-scale simulations over long-time scales on multicomponent systems.

The main trade-off is the two to three orders of magnitude higher computational cost of SNAP models compared to EAM. Nevertheless, it should be noted that SNAP models still scale linearly with the number of atoms and are orders of magnitude cheaper than DFT calculations. The combination of near-DFT accuracy at several orders of magnitude lower computational cost has enabled us to construct from first principles the high-temperature Ni-Mo phase diagram in Fig. 6(b), which is shown to be in excellent agreement with the experimental phase diagram. This effort, which requires long-time scale simulations of large MD simulation boxes exceeding 10 000 atoms, is beyond the scope of DFT calculations today. Most critically, the binary SNAP model is able to reproduce the correct formation energies and solubilities across a wide range of Ni-Mo structures (fcc, bcc, solid solutions, intermetallics, and surfaces), which is indicative of its general applicability to the study of microstructure and segregation phenomena in this highly important alloy system.

Finally, it is our belief that the development of potential models should account, on a holistic basis, for the trade-offs among prediction accuracy in energies, forces, and various properties, computational cost of the models, training data size, and extensibility beyond single-component systems.

ACKNOWLEDGMENTS

This work was primarily supported by the Office of Naval Research (ONR) Young Investigator Program (YIP) under Award No. N00014-16-1-2621. The CALPHAD and MC/MD investigations were supported by the Vannevar Bush Faculty Fellowship Program sponsored by the Basic Research Office of the Assistant Secretary of Defense for Research and Engineering and funded by the Office of Naval Research through Grant No. N00014-16-12569. The authors also acknowledge computational resources provided by Triton Shared Computing Cluster (TSCC) at the University of California, San Diego, the National Energy Research Scientific Computing Center (NERSC), and the Extreme Science and Engineering Discovery Environment (XSEDE) supported by the National Science Foundation under Grant No. ACI-1053575.

[1] J. Behler and M. Parrinello, Phys. Rev. Lett. **98**, 146401 (2007).

[2] A. P. Bartók, M. C. Payne, R. Kondor, and G. Csányi, Phys. Rev. Lett. **104**, 136403 (2010).

[3] M. Rupp, A. Tkatchenko, K.-R. Müller, and O. A. von Lilienfeld, Phys. Rev. Lett. **108**, 058301 (2012).

[4] A. P. Bartók, R. Kondor, and G. Csányi, Phys. Rev. B **87**, 184115 (2013).

[5] A. Thompson, L. Swiler, C. Trott, S. Foiles, and G. Tucker, J. Comput. Phys. **285**, 316 (2015).

[6] S. Chmiela, A. Tkatchenko, H. E. Sauceda, I. Poltavsky, K. T. Schütt, and K.-R. Müller, Sci. Adv. **3**, e1603015 (2017).

[7] T. D. Huan, R. Batra, J. Chapman, S. Krishnan, L. Chen, and R. Ramprasad, npj Comput. Mater. **3**, 1 (2017).

[8] J. Behler, J. Phys.: Condens. Matter **26**, 183001 (2014).

[9] W. J. Szlachta, A. P. Bartók, and G. Csányi, Phys. Rev. B **90**, 104108 (2014).

[10] F. Faber, A. Lindmaa, O. A. Von Lilienfeld, and R. Armiento, Int. J. Quantum Chem. **115**, 1094 (2015).

[11] M. Rupp, R. Ramakrishnan, and O. A. Von Lilienfeld, J. Phys. Chem. Lett. **6**, 3309 (2015).

[12] C. Chen, Z. Deng, R. Tran, H. Tang, I.-H. Chu, and S. P. Ong, Phys. Rev. Mater. **1**, 043603 (2017).

[13] N. Artrith, A. Urban, and G. Ceder, Phys. Rev. B **96**, 014112 (2017).

[14] J. S. Smith, O. Isayev, and A. E. Roitberg, Chem. Sci. **8**, 3192 (2017).

[15] S. Faraji, S. A. Ghasemi, S. Rostami, R. Rasoulkhani, B. Schaefer, S. Goedecker, and M. Amsler, Phys. Rev. B **95**, 104105 (2017).

[16] B. Kolb, X. Luo, X. Zhou, B. Jiang, and H. Guo, J. Phys. Chem. Lett. **8**, 666 (2017).

[17] V. L. Deringer and G. Csányi, Phys. Rev. B **95**, 094203 (2017).

[18] P. Rowe, G. Csányi, D. Alfè, and A. Michaelides, Phys. Rev. B **97**, 054303 (2018).

[19] V. L. Deringer, D. M. Proserpio, G. Csányi, and C. J. Pickard, Faraday Discuss (2018), doi:10.1039/C8FD00034D.

[20] D. Dragoni, T. D. Daff, G. Csányi, and N. Marzari, Phys. Rev. Mater. **2**, 0138082 (2017).

[21] J. Behler, R. Martoňák, D. Donadio, and M. Parrinello, Phys. Rev. Lett. **100**, 185501 (2008).

[22] R. Z. Khaliullin, H. Eshet, T. D. Kühne, J. Behler, and M. Parrinello, Phys. Rev. B **81**, 100103 (2010).

[23] H. Eshet, R. Z. Khaliullin, T. D. Kühne, J. Behler, and M. Parrinello, Phys. Rev. Lett. **108**, 115701 (2012).

[24] N. Artrith, T. Morawietz, and J. Behler, Phys. Rev. B **83**, 153101 (2011).

[25] N. Artrith and A. Urban, Comput. Mater. Sci. **114**, 135 (2016).

[26] G. C. Sosso, G. Miceli, S. Caravati, J. Behler, and M. Bernasconi, Phys. Rev. B **85**, 174103 (2012).

[27] W. Li, Y. Ando, E. Minamitani, and S. Watanabe, J. Chem. Phys. **147**, 214106 (2017).

[28] M. A. Wood and A. P. Thompson, J. Chem. Phys. **148**, 241721 (2018).

[29] R. Kobayashi, D. Giofré, T. Junge, M. Ceriotti, and W. A. Curtin, Phys. Rev. Mater. **1**, 053604 (2017).

[30] N. Artrith, A. Urban, and G. Ceder, J. Chem. Phys. **148**, 241711 (2018).

[31] N. V. Krstajić, V. D. Jović, L. Gajić-Krstajić, B. M. Jović, A. L. Antozzi, and G. N. Martelli, Int. J. Hydrogen Energy **33**, 3676 (2008).

[32] M. Donten, H. Cesiulis, and Z. Stojek, Electrochim. Acta **50**, 1405 (2005).

[33] Q. Han, S. Cui, N. Pu, J. Chen, K. Liu, and X. Wei, Int. J. Hydrogen Energy **35**, 5194 (2010).

[34] J. Hu, Y. N. Shi, X. Sauvage, G. Sha, and K. Lu, Science **355**, 1292 (2017).

[35] S. Plimpton, J. Comput. Phys. **117**, 1 (1995).

[36] F. Pedregosa, G. Varoquaux, A. Gramfort, V. Michel, B. Thirion, O. Grisel, M. Blondel, P. Prettenhofer, R. Weiss, V. Dubourg, J. Vanderplas, A. Passos, D. Cournapeau, M. Brucher, M. Perrot, and É. Duchesnay, J. Mach. Learn. Res. **12**, 2825 (2011).

[37] F. Neri and V. Tirronen, Artificial Intelligence Rev. **33**, 61 (2010).

[38] E. Jones, T. Oliphant, and P. Peterson SCIPY package (2014).

[39] M. de Jong, W. Chen, T. Angsten, A. Jain, R. Notestine, A. Gamst, M. Sluiter, C. Krishna Ande, S. van der Zwaag, J. J. Plata, C. Toher, S. Curtarolo, G. Ceder, K. A. Persson, and M. Asta, Sci. Data **2**, 150009 (2015).

[40] R. Tran, Z. Xu, B. Radhakrishnan, D. Winston, W. Sun, K. A. Persson, and S. P. Ong, Sci. Data **3**, 160080 (2016).

[41] G. L. W. Hart and R. W. Forcade, Phys. Rev. B **77**, 224115 (2008).

[42] J. P. Perdew, K. Burke, and M. Ernzerhof, Phys. Rev. Lett. **77**, 3865 (1996).

[43] G. Kresse and J. Furthmüller, Phys. Rev. B **54**, 11169 (1996).

[44] P. E. Blöchl, Phys. Rev. B **50**, 17953 (1994).

[45] S. P. Ong, W. D. Richards, A. Jain, G. Hautier, M. Kocher, S. Cholia, D. Gunter, V. L. Chevrier, K. A. Persson, and G. Ceder, Comput. Mater. Sci. **68**, 314 (2013).

[46] A. Jain, S. P. Ong, W. Chen, B. Medasani, X. Qu, M. Kocher, M. Brafman, G. Petretto, G.-M. Rignanese, G. Hautier, D. Gunter, and K. A. Persson, Concurr. Comp. Pract. E. **27**, 5037 (2015).

[47] J. R. Morris, C. Z. Wang, K. M. Ho, and C. T. Chan, Phys. Rev. B **49**, 3109 (1994).

[48] H. L. Lukas, S. G. Fries, B. Sundman *et al.*, *Computational Thermodynamics: The Calphad Method* (Cambridge University Press, Cambridge, UK, 2007), Vol. 131.

[49] S. L. Chen, F. Zhang, F. Y. Xie, S. Daniel, X. Y. Yan, Y. A. Chang, R. Schmid-Fetzer, and W. A. Oates, JOM **55**, 48 (2003).

[50] K. Frisk, Calphad **14**, 311 (1990).

[51] https://github.com/materialsvirtuallab/snap.

[52] See Supplemental Material at http://link.aps.org/supplemental/10.1103/PhysRevB.98.094104 for SNAP coefficients of Ni, Cu, and Ni-Mo systems, Cu SNAP potential performance, as well as phonon dispersion curves of Ni, Ni_3Mo, and Ni_4Mo with different potentials.

[53] H. M. Ledbetter, Phys. Status Solidi A **66**, 477 (1981).

[54] H. W. Sheng, M. J. Kramer, A. Cadien, T. Fujita, and M. W. Chen, Phys. Rev. B **83**, 134118 (2011).

[55] X. W. Zhou, R. A. Johnson, and H. N. G. Wadley, Phys. Rev. B **69**, 144113 (2004).

[56] E. Asadi, M. Asle Zaeem, S. Nouranian, and M. I. Baskes, Acta Mater. **86**, 169 (2015).
[57] R. Hill, Proc. Phys. Soc., London, Sect. A **65**, 349 (1952).
[58] G. Alers, J. Neighbours, and H. Sato, J. Phys. Chem. Solids **13**, 40 (1960).
[59] E. H. Megchiche, S. Pérusin, J.-C. Barthelat, and C. Mijoule, Phys. Rev. B **74**, 064111 (2006).
[60] G. Henkelman, B. P. Uberuaga, and H. Jónsson, J. Chem. Phys. **113**, 9901 (2000).
[61] G. Simmons and H. Wang, *Single Crystal Elastic Constants and Calculated Aggregate Properties* (MIT Press, Cambridge, MA, 1971).
[62] R. E. W. Casselton and W. Hume-Rothery, J. Less-Common Met. **7**, 212 (1964).